

3.1.2 Polarization observables

In this subsection, I will present my predictions for the selected polarization observables in the deuteron photodisintegration process at two photon energies: $E_\gamma = 30 \text{ MeV}$ and $E_\gamma = 100 \text{ MeV}$. A priori, various polarization states and measurements are thinkable for the $\gamma + d$ scattering. Polarization of the target deuteron leads to the deuteron analyzing power. Similarly using the polarized photons results in the photon asymmetry measurements. Using both polarized photon and deuteron allows for spin correlation measurement. Finally, detecting the spin polarization of at least one nucleon in the final state would deliver final polarization or spin transfer coefficients. However, such experiments are very challenging and, up to my best knowledge, have not been done yet at regarded here photon energies. Thus, in the following, I will restrict myself to results for polarization observables arising from the polarization of the initial particles.

I start with deuteron vector iT_{11} and tensor T_{20} , T_{21} and T_{22} analyzing power, which arises from various spin states of the deuteron.

Deuteron tensor analyzing powers can be calculated via cross section as it is defined in [71]:

$$\frac{d\sigma}{d\Omega} = \frac{d\sigma_0}{d\Omega} \left\{ 1 - \sqrt{3/4} P_z \sin \theta_H \sin \phi_H T_{11} + \sqrt{1/2} P_{zz} [(3/2 \cos^2 \theta_H - 1/2) T_{20} - \right. \\ \left. - \sqrt{3/8} \sin 2\theta_H \cos \phi_H T_{21} + \sqrt{3/8} \sin^2 \theta_H \cos 2\phi_H T_{22}] \right\}, \quad (3.2)$$

where σ_0 is the unpolarized cross section, P_z (P_{zz}) the vector (tensor) target polarization, θ_H - the angle between polarization axis and photon momentum, and ϕ_H - is the angle between the polarization plane (containing the polarization axis and momentum of the photon), and the reaction plane (containing the momenta of the proton and neutron).

In the Figures 3.6(a,b) and 3.7(a,b) I show my predictions at $E_\gamma = 30 \text{ MeV}$, for the T_{20} , T_{21} , T_{22} and iT_{11} respectively as functions of the outgoing proton momentum polar angle θ_p in the centre of the mass (CM) frame. Each of them is organized in a similar way: the top panel shows a dependence of the predictions on the chiral order of the potential. The middle subfigure is showing a correspondent truncation error for each of the predictions from a top row (except LO, because its uncertainty is too large and will spoil the clarity of the figure). The last (bottom) panel shows the cut-off dependence at the chiral order N^4LO^+ . All results have been obtained using 1NC–Siegert model of nuclear current.

All the analyzing powers presented here show excellent convergence upon a chiral order as it is hard to distinguish the predictions from each subsequent order starting from the N^2LO . The relative width of the N^4LO^+ truncation band for T_{20} , T_{21} and T_{22} are 0.06 %, 0.05 % and 0.19 %, respectively (at $\theta_p = 90^\circ$, 60° and 90° , respectively). The slowest convergence is observed for iT_{11} (Fig. 3.7b) where we can recognize N^2LO band in the figure. Nevertheless, at the N^4LO^+ the width truncation band at $\theta_p = 20^\circ$ (maximum point) is only a 0.2 %. The cut-off dependence for all regarded observables is weak and predictions for each value of the Λ are hardly separable with the naked eye. The relative spread of the predictions based on various Λ at the same angles as above are 0.87 %, 0.94 %, 3.42 % and 0.68 % for T_{20} , T_{21} , T_{22} and iT_{11} , respectively.

Corresponding predictions at the photon energy $E_\gamma = 100 \text{ MeV}$ (Figs. 3.8 and 3.9) preserve similar trends for each observable. In general, predictions are being converged starting even from the N^2LO and only for the iT_{11} I find that truncation error's bands

are noticeably wide even at N⁴LO and N⁴LO⁺. Cutoff dependence at this energy is a bit stronger compared to those at E _{γ} = 30 MeV, especially for T₂₂ and iT₁₁ analyzing powers (Fig. 3.9 vs Fig. 3.7), where one can see the slightly stronger discrepancy at the maxima and minima points.

The choice of Λ does not affect predictions substantially even at that higher energy: the relative spread among all cut-offs for T₂₀ is 1.54% around the point of maximum ($\theta_p = 90^\circ$). For other components of the tensor analyzing power spread amounts up to: 0.14% at $\theta_p = 60^\circ$ for T₂₁; 3.68% at $\theta_p = 90^\circ$ for T₂₂; and 4.91% at $\theta_p = 75^\circ$ for iT₁₁. We see again that iT₁₁ has much larger spread in the maximum and is more sensitive to the cut-off choice. However, summarizing my findings for the deuteron tensor analyzing powers, I conclude that cut-off dependence is generally weak also at E _{γ} = 100 MeV.

Turning our attention to the chiral order convergence, we observe that predictions are mostly converged starting either from N²LO or N³LO. The relative width of N⁴LO⁺ truncation band for T₂₀, T₂₁ and T₂₂ are 0.7%, 0.7% and 0.04% respectively (at the same angles as used above). Another case is iT₁₁, for which this width is much larger: 6.8% at $\theta_p = 20^\circ$. The truncation uncertainty for all analyzing powers is much lower than one, related to the choice of the cut-off parameter. However, iT₁₁ seems to be more sensitive both to the choice of the cut-off parameter and to the chiral order than other regarded observables. Even for iT₁₁, the cut-off spread is almost twice larger than the truncation error. Standing out of other tensor components, iT₁₁ can be useful for the investigation of the cut-off dependence of the model. Of course, we can repeat once more that our model is less accurate at higher energies which is reflected in a stronger cut-off dependence and slower chiral convergence. However, I conclude that even at these higher energies tensor analyzing powers are well converged with respect to the chiral order.

Comparison of the predictions obtained using the chiral N⁴LO⁺ potential $\Lambda = 450$ MeV with ones obtained taking AV18 potential show a very good agreement: the relative difference at E _{γ} = 30 MeV is below 6% for the regarded tensor analyzing powers at specified angles. Picture at E _{γ} = 100 MeV is even better: the difference does not exceed 4% for all observables and a whole range of scattering angles.

In Fig. 3.10 together with our most advanced "Full" predictions (N⁴LO⁺, $\Lambda = 450$ MeV, the Siegert theorem), at E _{γ} = 30 MeV I show predictions obtained with 1NC only and the Siegert predictions but with plane-wave contribution without rescattering part. In the case of deuteron's tensor analyzing power components, the contribution of rescattering part is important for T₂₀, T₂₁ and T₂₂ (the relative difference is up to 20% in extremes) and crucial for iT₁₁ where the PW part equals to zero. The 2NC component taken into account via Siegert theorem has a dominant contribution here. We see that 1NC predictions are absolutely away from the "Full" predictions and in the case of iT₁₁ it does not even reflect complete prediction qualitatively.

Fig. 3.11 presents similar results but for E _{γ} = 100 MeV and it is interesting that the difference between Full and 1NC prediction becomes smaller and it is especially visible for T₂₂. At this energy, the relative difference between "Full" and 1NC predictions at $\theta_p = 90^\circ$ is 43.6% compared to 122.8% at E _{γ} = 30 MeV. Similarly, the difference for T₂₀ at E _{γ} = 30 MeV ($\theta_p = 90^\circ$) is 91.4% and at E _{γ} = 100 MeV it drops to 28.8%. This may also be affected by the fact that values at $\theta_p = 90^\circ$ are quite small for the Full prediction, nevertheless, the difference still becomes smaller at the E _{γ} = 100 MeV. This trend is noticeable by looking also on the results presented below. Nevertheless, in both cases 2NC (via the Siegert) brings sufficient contributions and cannot be omitted for obtaining the full picture.

Important

check if
is PW defined?

In the following figures, I will compare my predictions with experimental data. In some cases, I will keep a similar way as it was done in [71] where due to experimental conditions results are given not at single photon energy, but for a specific ranges of E_γ . In the Figures 3.12 - 3.18 I show an angular dependence of the T_{2i} ($i = 0, 1, 2$) for a specific energy bands: 25–45 MeV, 45–70 MeV, 70–100 MeV, and 230–330 MeV. The solid blue line shows an average value of the observable in the specified energy intervals: obtained at N^4LO^+ with $\Lambda = 450$ MeV, while the pink dashed line is a prediction obtained with the same setup but without using contributions from Siegert approach (single nucleon current only). Bands for each prediction specify the spread of predictions due to the energy band ~~in different range~~.

One clearly sees that the data description is better for the predictions with Siegert contributions included and the 1NC alone is not able to describe the experiment properly. Our Full model nicely describes data up to $E_\gamma = 70$ MeV. With increasing energy (above 100 MeV), the difference between predicted values and experimental data becomes larger (especially for T_{22}), which shows a necessity of improving the theoretical model before applying it to higher energies. Nevertheless, even with approximations used, the data description remains reasonable. We observe that quite often and in particular in Fig. 3.17 and Fig. 3.18 the data description is worse for smaller angles. Especially for the tensor analyzing power T_{22} the group of data point lying closer to $\theta_p = 30^\circ$ are farther from the theoretical prediction than ~~the~~ second group. In Fig. 3.18 the description of data points for T_{20} seems to be better with the 1NC (dashed line), but in this case, it is only an accidental match as we do not observe similar trend for any other angular range or for different observables. In addition, experimental uncertainties are larger at small angles, and in all cases our description is inside 3σ uncertainty.

In the Figure 3.19 the energy dependence of T_{20} and T_{22} at specific angle $\theta_p = 88^\circ$ is presented for the energy range 0–400 MeV. Besides my predictions I also demonstrate the experimental data from [71] and [74] as well as theoretical calculations from [75]. For T_{20} all models are able to describe experimental data well, even for high energies. On the other hand, T_{22} is not described so well: for the energies below 140 MeV the predictions are within uncertainties of experimental data, but further the difference with the data increases. Above 140 MeV Full predictions do not reflect the qualitative nature of the data. Namely, I observe that data points start ascending which is not represented in my predictions. Theoretical predictions from [75] (brown dashed curve) are also not able to describe data quantitatively for T_{22} , but increasing of T_{22} towards data is present. The predictions in [75] are obtained with a one-body current using the Bonn one-boson-exchange potential in coordinate space (OBEP) NN potential with the major part of meson exchange currents (MEC) included implicitly via the Siegert operators plus explicit pion exchange currents (MEC), isobar configurations (IC) and the leading order of relativistic corrections (RC). So authors use a different potential, but probably the main difference in predictions is coming from the more advanced model of the current operator and the RC included there. We see that experimental errors are quite large which is not so surprising giving that the experiment was conducted back in 1989. New experiments would be a great support in development of the nuclear interactions as we expect relativistic calculations in the future [76].

The Fig. 3.20 presents ~~similar~~ results to the Fig. 3.19 but with various values of the cutoff parameter. The deviation between these predictions is rather small (especially below 150 MeV), while the difference with the calculation from [75] and experimental data remains as discussed above.

analyzers

those given in

and currents

Where

with the

 θ_p 

Similar picture is seen in the Figures 3.21 and 3.22 where I show an energy dependence of the mean of deuteron analyzing powers over specific angular ranges (following the data from [71]). In Fig. 3.21 we see that only predictions for T_{20} are able to reflect the experimental results, while for T_{21} and T_{22} my results are reasonable (quantitative wise) only for lower energies and difference in data becomes larger when energy increases. Predictions for T_{21} and T_{22} once more confirm an insufficiency of 1NC and the importance of 2-nucleon current contributions. The description is better for bigger angles Fig. 3.22): at lower energies (below 140 MeV) the correspondence to experimental data is good for all three observables but above that threshold, all predictions (especially for T_{22}) move away from the ~~measurement~~ data. Again, big uncertainty of the data calls for the experiment to be repeated.

presented

conclude

that

In the Fig. 3.23 I demonstrate predictions for the photon asymmetry Σ_γ for the deuteron photodisintegration with $E_\gamma = 20$ MeV (a) and 60 MeV(b) together with the experimental data of [77–80]. Both (a) and (b) figures are organized similarly to the figures I showed above for the tensor analyzing powers (e.g. Fig. 3.7). That is the top panel is aimed to demonstrate predictions obtained with the chiral SMS potential at different orders of the chiral expansion, the middle one shows a truncation error and the bottom one shows the cut-off dependence. For that observable we see an excellent convergence with respect to the chiral order. For both regarded energies predictions at different orders are very close to each other except the LO and NLO curves. Nevertheless, at $E_\gamma = 60$ MeV the truncation error bands reveal some uncertainty connected with the chiral order and it is expected that even some higher chiral orders would still contribute to the predictions at this energy. The relative width of the truncation band are 0.26 %, 5.04 %, 5.05 %, 5.73 % and 14.96 % for N^4LO^+ , N^4LO , N^3LO , N^2LO and NLO respectively and at $\theta_p = 90^\circ$.

The cut-off dependence is also much stronger at 60 MeV. One clearly sees that predictions are different for various values of the Λ . The relative difference between predictions to the cut-off parameter at 20 MeV is 0.26 % while at the photon energy 60 MeV it is 4.41 % (both calculated at $\theta_p = 90^\circ$). So the theoretical uncertainty related to regulator value is nearly 17 times bigger than due to the truncation error ($4.11/0.26 = 16.96$).

Comparing my predictions to experimental data, I observe that for the lower energy predictions are almost perfectly overlapping with experimental points within the error bars. For a few data points our predictions are outside data error bars, but they are still within 3σ range. For 60 MeV, experimental data points are systematically below theoretical curves, especially in the middle of the angular range. It seems that some systematic uncertainty is presented in predictions and ad hoc multiplication by some factor (around 0.8) could help predictions be more similar to ~~the~~ experimental data. But very likely the observed discrepancy points to the simplified character of the model used here. ~~in my calculations.~~ together with

In the Fig. 3.24 the predictions obtained with the Full set of components (plane wave – rescattering and 1NC + Siegert, solid blue curve) are shown versus predictions obtained without rescattering (green dashed-dotted line) and without contribution from the Siegert (pink dashed line) for the same photon energies as above: $E_\gamma = 20$ MeV (left panel) and $E_\gamma = 60$ MeV (right panel). For the $E_\gamma = 20$ MeV the difference between Full and PW is quite small, whereas 1NC ~~is~~ noticeably differs from the Full prediction, especially around the smallest and largest angle values. For the $E_\gamma = 60$ MeV the difference between such predictions is larger: we see not only quantitative, but also qualitative variations. The 1NC curve has much larger values and its shape becomes more asymmetric with respect to the $\theta_p = 90^\circ$ point.

with the same current but

but keeping rescattering

bigger

In the Fig. 3.25 (left) I present a dependence of the photon asymmetry Σ_γ on the photon energy at a fixed value of the outgoing proton polar direction $\theta_p = 90^\circ$ (following the data given at [81] and [78]). It is noticeable that with increasing energy, the predictions are systematically above the experimental data and the discrepancy ~~grows~~¹ with energy. This trend was also observed in the angular dependence of the asymmetry at 60 MeV so I conclude that within our framework, Σ_γ is sensitive to the initial photon energy and some theoretical contributions are missing to get satisfactory predictions at higher energies. From the Fig. 3.25 we can say that large discrepancy with data starts already above $E_\gamma = 35$ MeV.¹

The right panel of the Fig. 3.25 shows an impact of the different model components to the obtained predictions. We see that the difference between the Full predictions (solid blue line) and the one obtained with a 1NC only (without the Siegert contribution) is larger than the difference with predictions with plane-wave part only (without rescattering). Both these incomplete predictions are farther from the experimental data, (for PW at larger energies only) and have a different curve shape~~s~~ as well.

The proton polarization is demonstrated in Fig. 3.26 for the photon energy 30 MeV(a) and 100 MeV(b). In this case even at higher energy (such as 100 MeV) predictions reveal neither slower convergence concerning the chiral order nor stronger cut-off dependence. Figures for both energies show that only next-to-leading order brings a relatively high contribution while taking into account other subsequent orders does not change predictions significantly. In the case of the cut-off dependence, we see that curves for each value of Λ are very close to each other. The relative difference of the predictions with respect to the cut-off parameter is 4.04 % at the minimum point $\theta_p = 130^\circ$ of $E_\gamma = 30$ MeV and 5.62 % at $\theta_p = 160^\circ$ and $E_\gamma = 100$ MeV. The dependence is slightly stronger for higher energy, but both values are comparable. Again, the cut-off-related uncertainty exceeds the truncation error.

Predictions for the neutron polarization at the energies 2.75 MeV and 100 MeV are shown in the Fig. 3.27. The choice of energy is conditioned by the availability of experimental data, which were taken in 1965 in Livermore [82] and in 1986 at TRIUMF [83]. In the case of $E_\gamma = 2.75$ MeV (Fig. 3.27a), we see that predictions reflect the behavior of experimental data points qualitatively, having more or less a constant offset of the values. A similar offset was obtained also in [19], where various approaches were presented. Authors compare different models which leads to very similar theoretical results even though different potentials are used with and without relativistic correction. One of the theoretical predictions is included even in the experimental papers [82] and authors state that there might be a systematic error in the calibration of the analyzing power of the neutron polarimeter which could affect experimental results precision. Interestingly, predictions clearly show a symmetrical form of the curve, while the experimental data have some deviations from the symmetrical form. ~~This~~ ^{These} ~~subsets~~ ^{subsets} can be a sign that some problem with the data can be in this case (taking into account also that the experiment had been done in 1965). In [82] authors even make a plot of the theoretical curve multiplied by the factor 0.879 which almost perfectly overlaps with experimental data afterward.

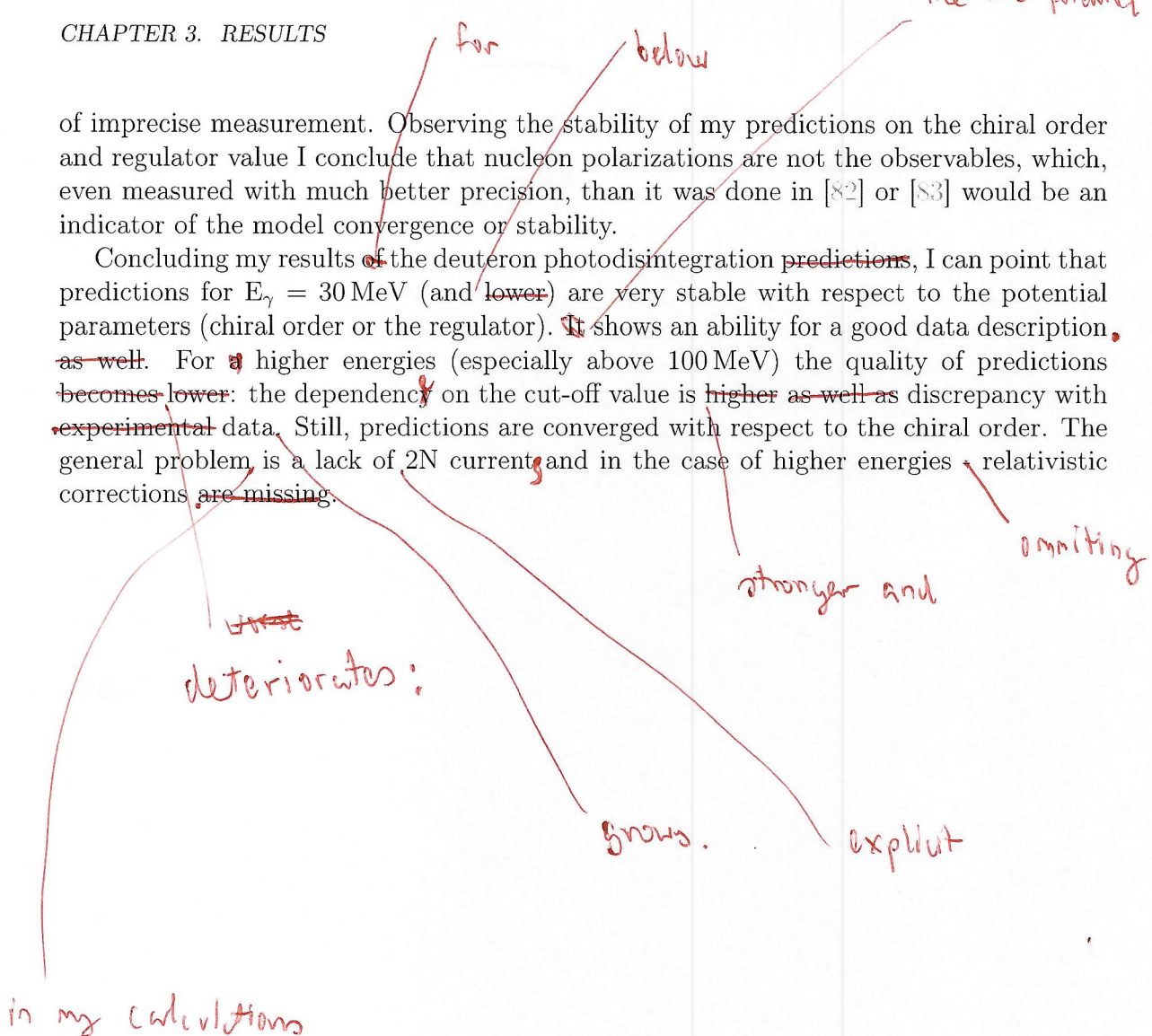
At the energy $E_\gamma = 100$ MeV (Fig. 3.27b) my predictions describe the data very well. For most of the data points, predicted values are within error bars, and only some of the points (e.g. around 50°) have a prediction in distance more than one standard deviation. Nevertheless, these data points look like they are out of general trend and may be a result

¹It is worth to note that data of [78] are above these from [81] (however still inside 3σ experimental error bands) and remain in agreement with my predictions even at $E_\gamma = 60$ MeV.

can be
in main
text →

of imprecise measurement. Observing the stability of my predictions on the chiral order and regulator value I conclude that nucleon polarizations are not the observables, which, even measured with much better precision, than it was done in [82] or [83] would be an indicator of the model convergence or stability.

Concluding my results of the deuteron photodisintegration predictions, I can point that predictions for $E_\gamma = 30 \text{ MeV}$ (and lower) are very stable with respect to the potential parameters (chiral order or the regulator). It shows an ability for a good data description, as well. For higher energies (especially above 100 MeV) the quality of predictions becomes lower: the dependency on the cut-off value is higher as well as discrepancy with experimental data. Still, predictions are converged with respect to the chiral order. The general problem is a lack of 2N currents and in the case of higher energies relativistic corrections are missing.



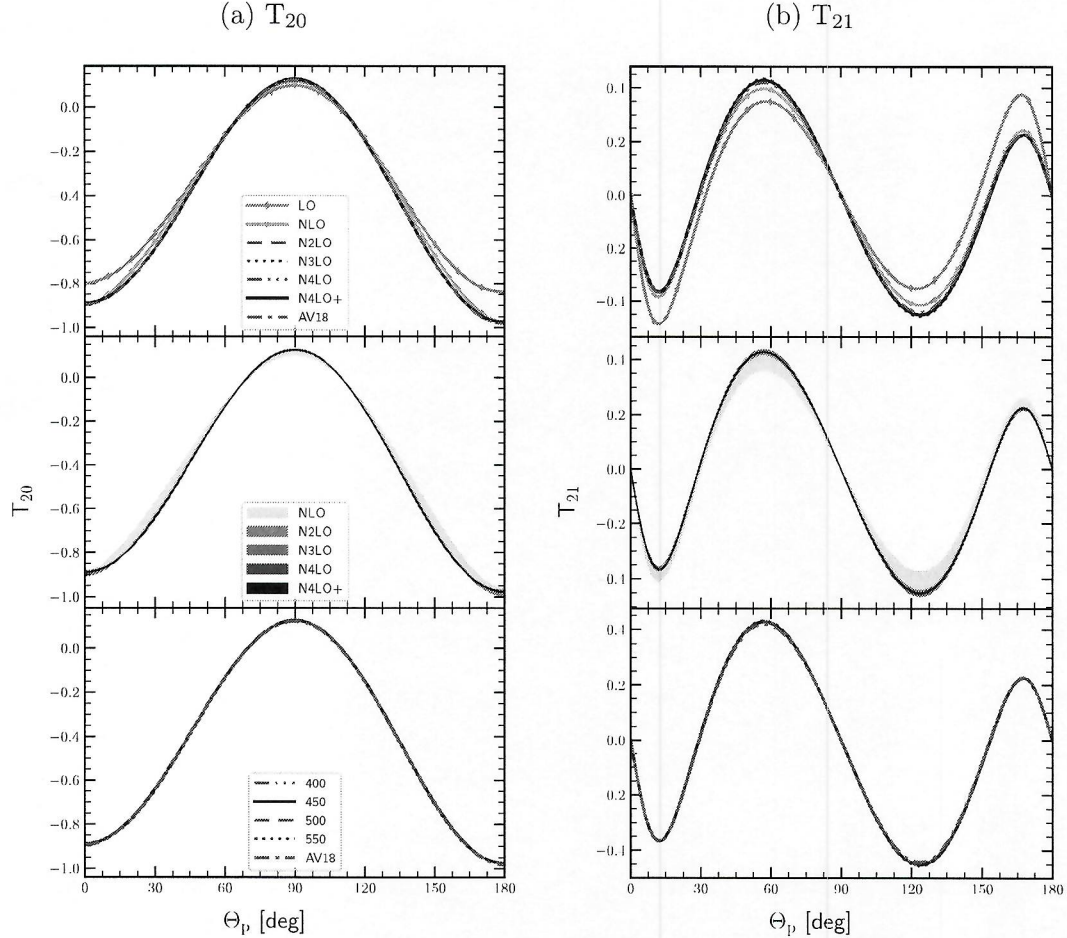


Figure 3.6: The deuteron tensor analyzing powers T_{20} (a) and T_{21} (b) as a function of the outgoing proton angle θ_p in the centre of the mass frame for the photon energy $E_\gamma = 30$ MeV. The top row presents results obtained using the SMS potential at different chiral orders (from LO to N^4LO^+) with the cut-off parameter $\Lambda = 450$ MeV. The middle row shows truncation errors for each chiral order starting from NLO , and the bottom row presents a cut-off dependence at N^4LO^+ . For the sake of comparison, predictions obtained with the AV18 potential are given as well. For all predictions 1NC–Siegert model is used.

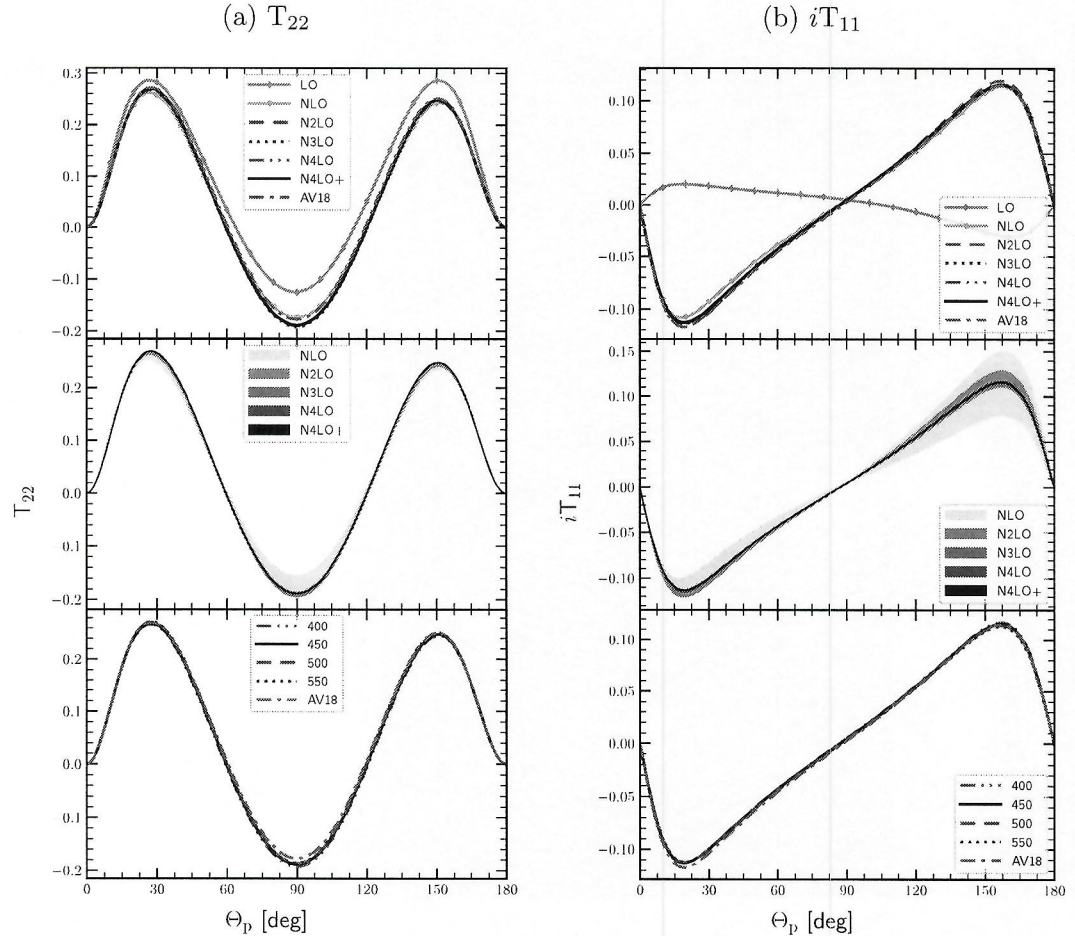


Figure 3.7: The same as in Fig. 3.6 but for the deuteron tensor analyzing power T_{22} (left column (a)) and the deuteron vector analyzing power iT_{11} (right column (b)).

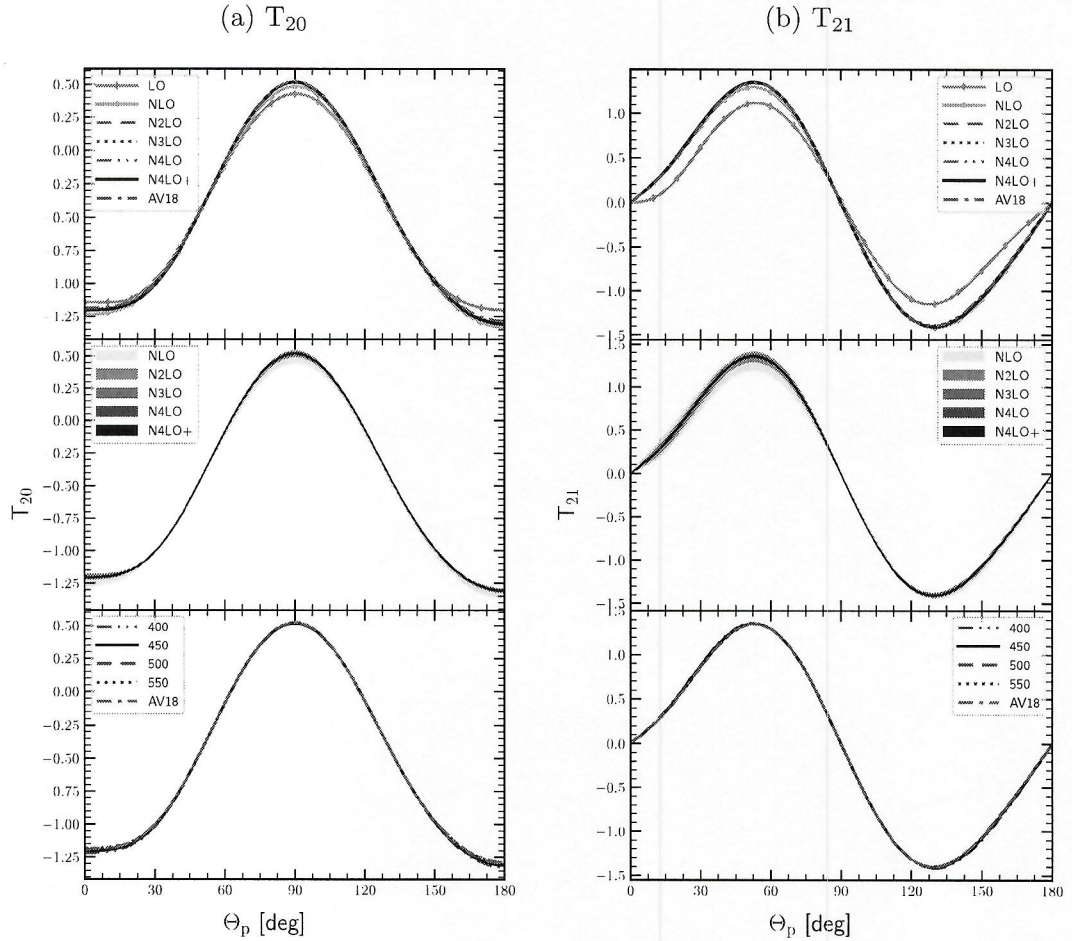


Figure 3.8: The deuteron tensor analyzing powers T_{20} (a) and T_{21} (b) as a function of the outgoing proton angle θ_p in the center of mass frame for the photon energy $E_\gamma = 100$ MeV. The top row presents results obtained using the SMS potential at different chiral orders (from LO to N^4LO^+) with the cut-off parameter $\Lambda = 450$ MeV. The middle row shows truncation errors for each chiral order starting from NLO, and the bottom row presents a cut-off dependence at N^4LO^+ . For the sake of comparison, predictions obtained with the AV18 potential are given as well. For all predictions 1NC+Siegert model is used.

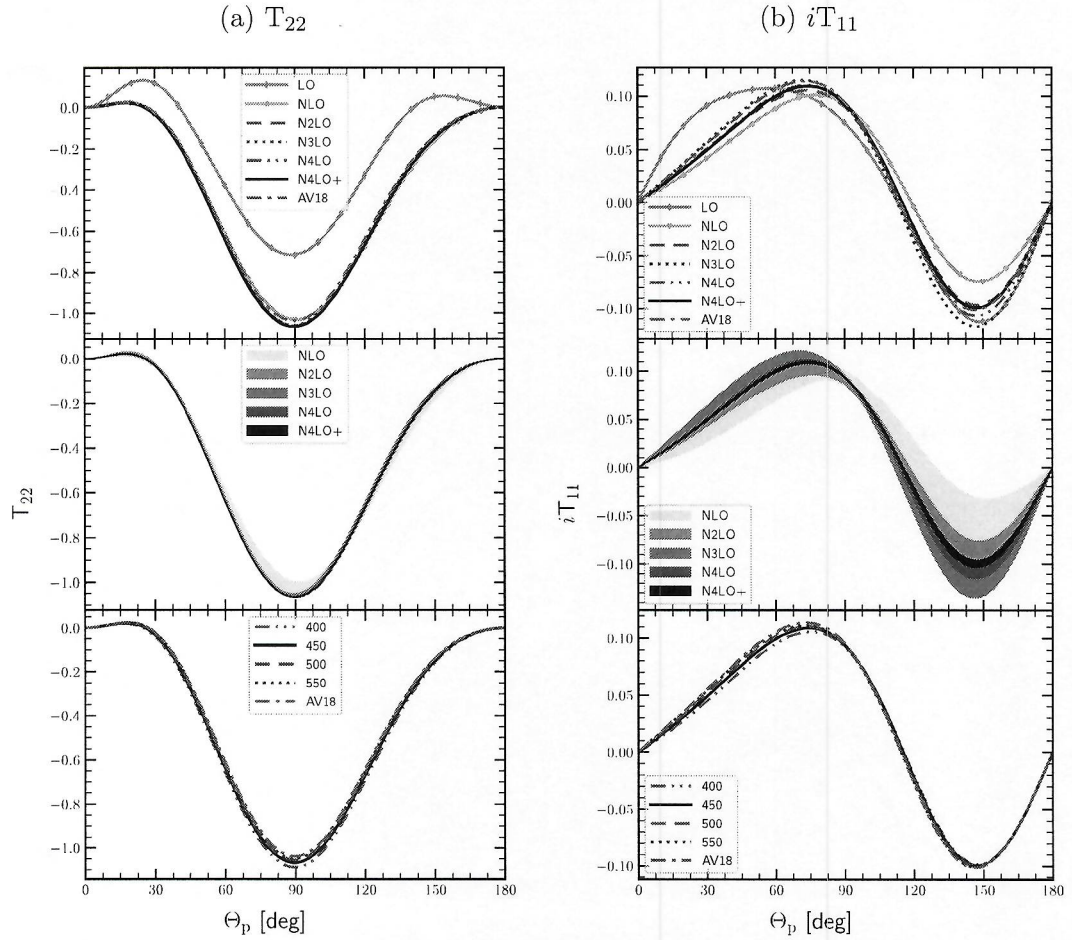


Figure 3.9: The same as in Fig. 3.8 but for the deuteron tensor analyzing power T_{22} (left column (a)) and the deuteron vector analyzing power iT_{11} (right column (b)).

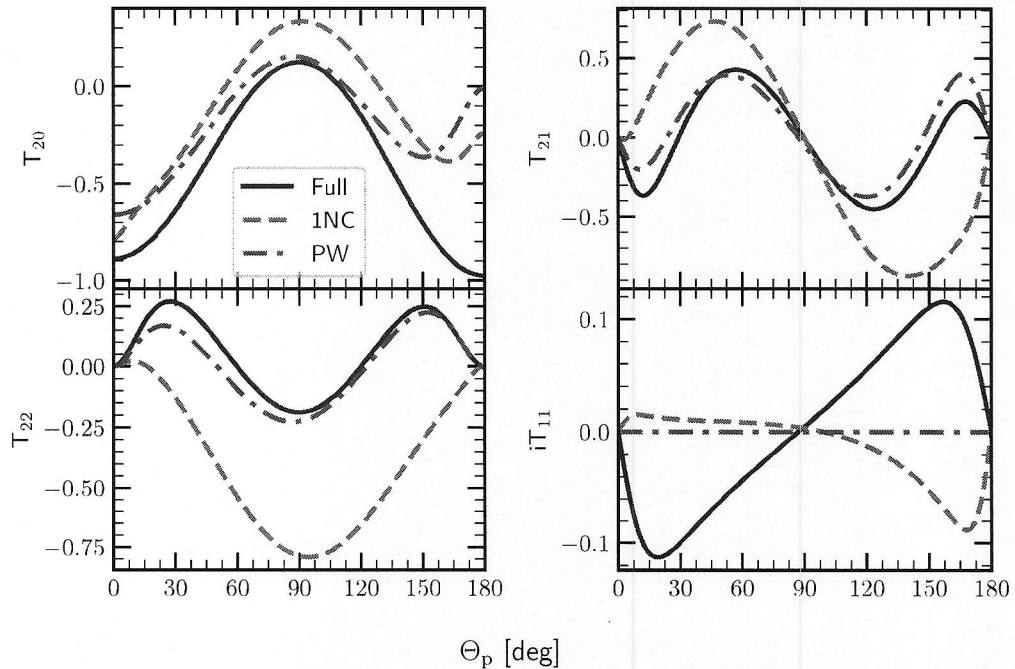


Figure 3.10: The deuteron tensor analyzing powers T_{20} , T_{21} , T_{22} and the deuteron vector analyzing power iT_{11} as a function of the outgoing proton angle θ_p in the CM frame at $E_\gamma = 30$ MeV. Similarly to Fig. 3.4b predictions obtained with chiral N^4LO^+ potential and $\Lambda = 450$ MeV are presented for three theoretical models. The blue solid line is the most complete prediction we have (plane-wave plus rescattering parts, 1NC + Siegert), the pink dashed line shows predictions obtained with single-nucleon current only (1NC) - without the Siegert contributions and the green dashed-dotted line is a prediction in which we neglect the rescattering part and stick to the plane-wave part only but keeping the Siegert contributions.

with plane-wave plus
rescattering ~~and~~ but

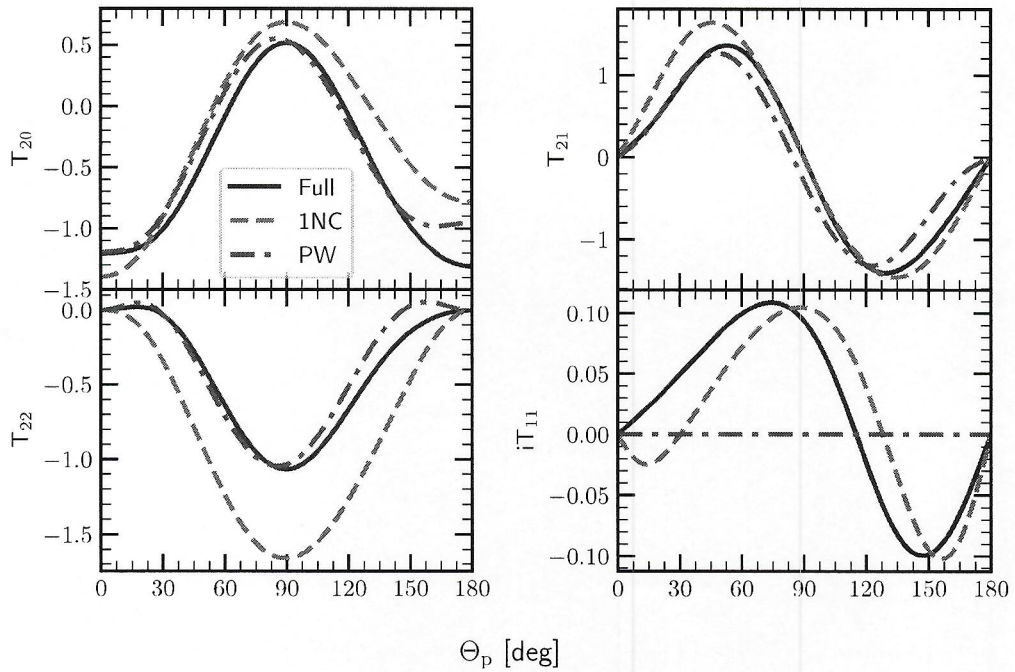
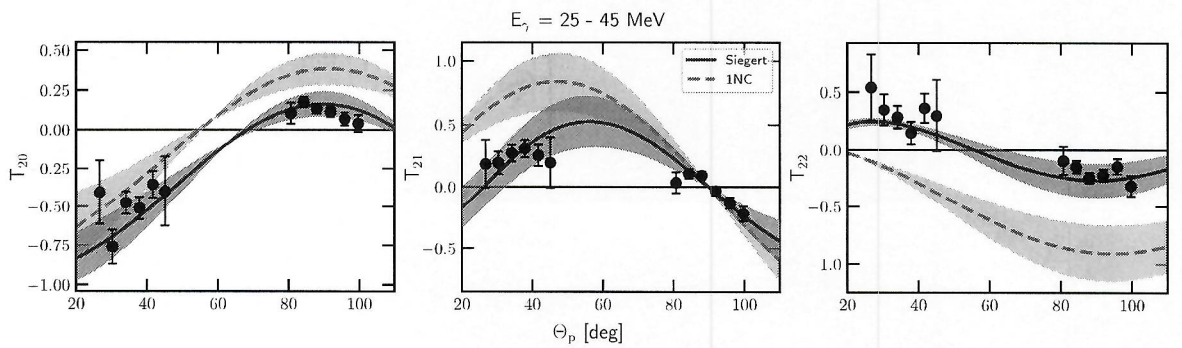

 Figure 3.11: The same as in Fig. 3.10 but for $E_\gamma = 100$ MeV.


Figure 3.12: Tensor analyzing powers T_{20} , T_{21} and T_{22} as a function of the outgoing proton angle θ_p in the CM frame. The solid blue line is the mean value of my predictions obtained at energy values from 25 to 45 MeV with the SMS potential at N^4LO^+ chiral order and with $\Lambda = 450$ MeV and with 1NC used together with the Siegert approach. The pink dashed line is a similar prediction but with the 1NC only. The corresponding bands show the limits of predictions in the regarded energy region. Filled circles are experimental data from [71] for the same energy range.

(step ... MeV)

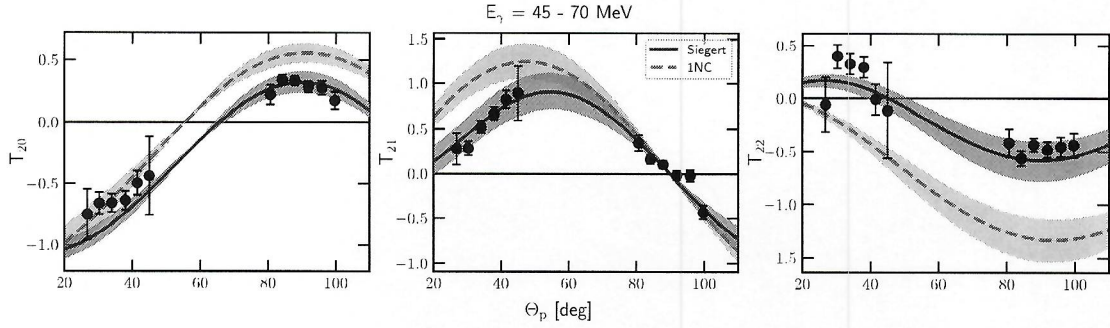


Figure 3.13: The same as in Fig. 3.12 but for energy bin $45 - 70 \text{ MeV}$.

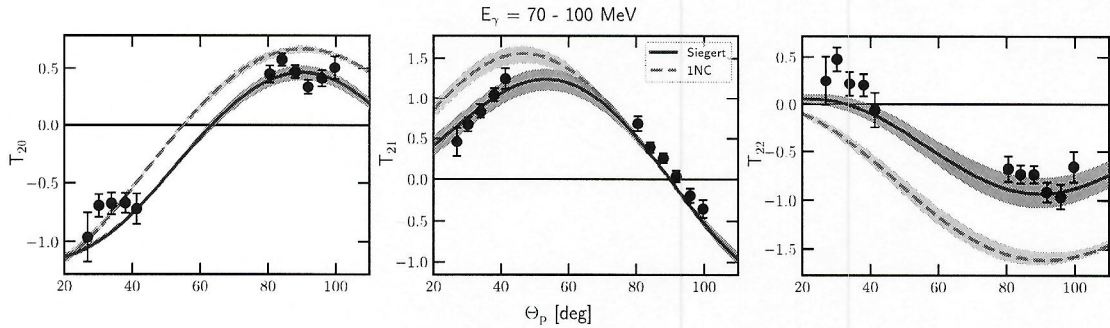


Figure 3.14: The same as in Fig. 3.12 but for energy bin $70 - 100 \text{ MeV}$.

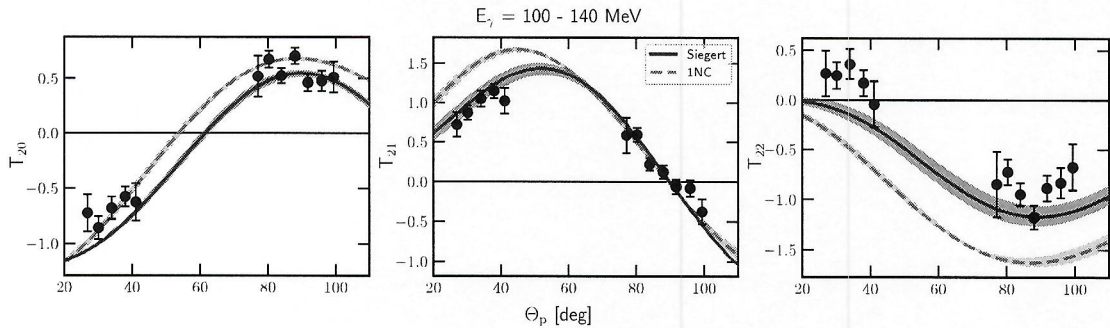


Figure 3.15: The same as in Fig. 3.12 but for energy bin $100 - 140 \text{ MeV}$.

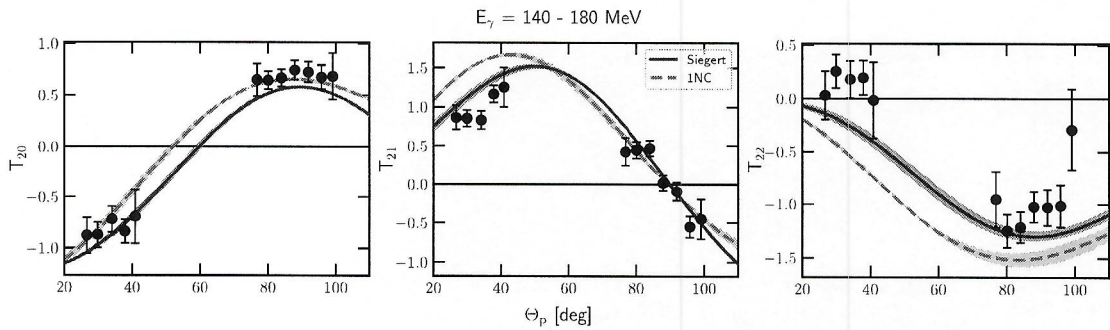


Figure 3.16: The same as in Fig. 3.12 but for energy bin $140 - 180 \text{ MeV}$.



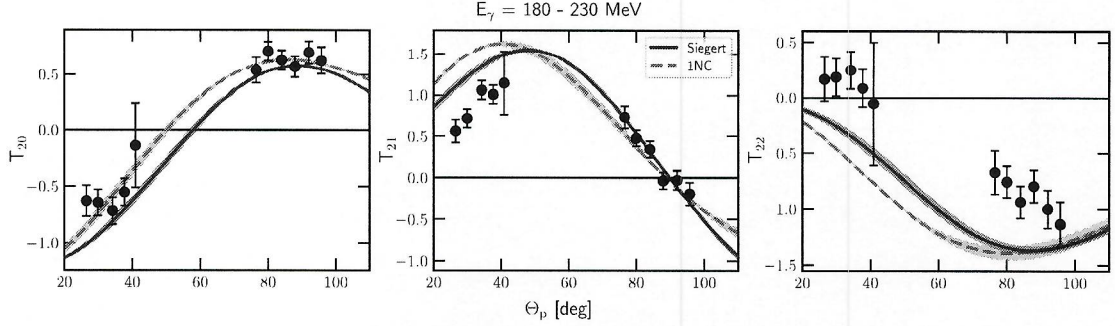
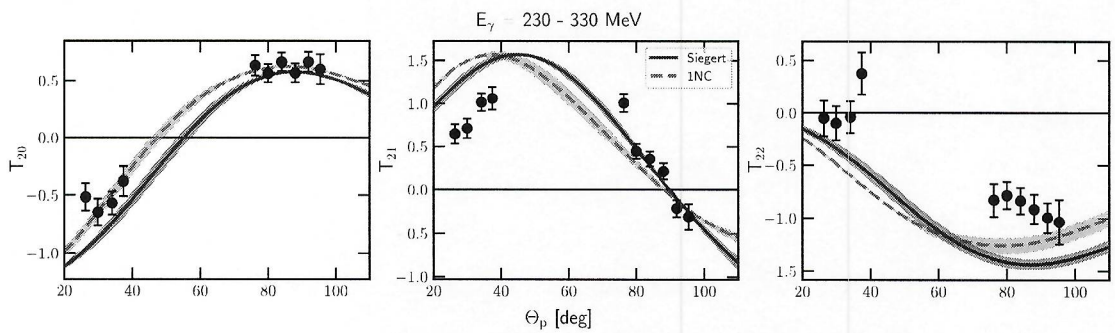
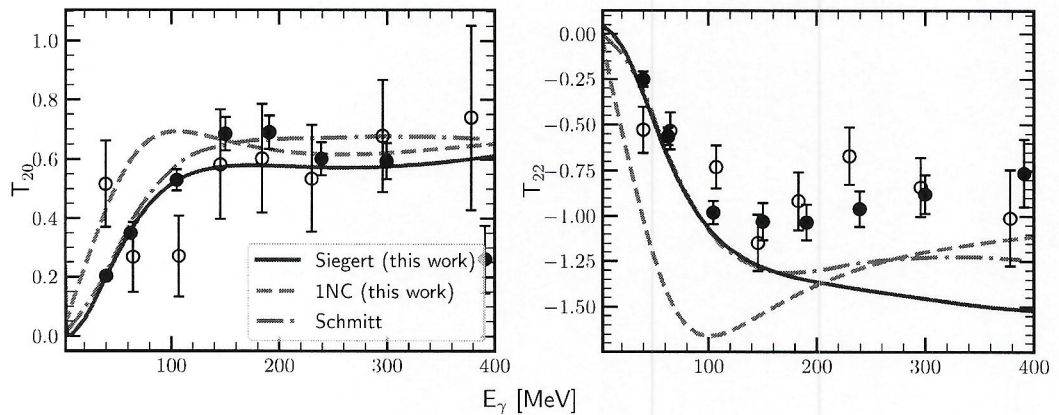

 Figure 3.17: The same as in Fig. 3.12 but for energy bin $180 - 230 \text{ MeV}$.

 Figure 3.18: The same as in Fig. 3.12 but for energy bin $230 - 330 \text{ MeV}$.


Figure 3.19: The tensor analyzing powers T_{20} (left) and T_{22} (right) as a function of the photon energy E_γ at fixed outgoing proton angle $\theta_p = 88^\circ$ in the center of mass frame. My predictions (blue solid line) are obtained with the SMS potential at the chiral order $N^4\text{LO}^+$, with the cut-off parameter $\Lambda = 450 \text{ MeV}$ and with 2NC contributions included via the Siegert theorem. The dashed pink curve shows predictions obtained with the same interaction but without 2NC contributions. The dashed-dotted brown curve presents theoretical results from [75]. Experimental data are taken from [71] (filled circles) and [74] (empty circles).

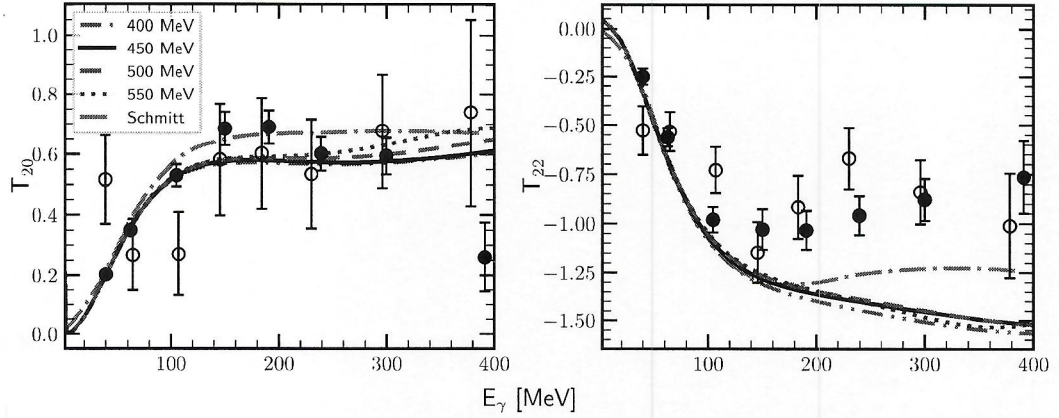


Figure 3.20: The tensor analyzing powers T_{20} (left) and T_{22} (right) as a function of the photon energy E_γ at fixed outgoing proton angle $\theta_p = 88^\circ$ in the center of mass frame. My predictions have been obtained with the SMS potential at the chiral order N^4LO^+ , with the different values of the cut-off parameter Λ (from 400 MeV to 550 MeV). The dashed-dotted brown curve presents theoretical results from [70]. Experimental data are taken from [71] (filled circles) and [74] (empty circles).

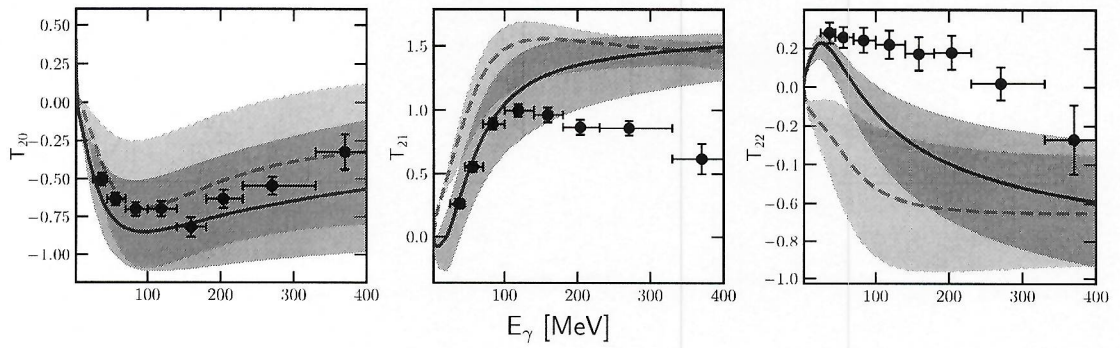


Figure 3.21: The averaged tensor analyzing powers T_{20} (left), T_{21} (middle) and T_{22} (right) as a function of the photon energy for the outgoing proton momentum polar angle θ_p in range $24^\circ - 48^\circ$ in the center of mass frame. The solid blue curve is a mean value of my predictions at energy values ranges from 25 to 45 MeV, obtained with the SMS potential at N^4LO^+ chiral order and with $\Lambda = 450$ MeV and with 1NC used together with the Siegert approach. The pink dashed curve represents similar predictions but with the nuclear current reduced to the 1NC only. The corresponding bands show predictions at border energies 25 and 45 MeV. The filled circles are experimental data from [71] for the same energy range.

(step ~ MeV)

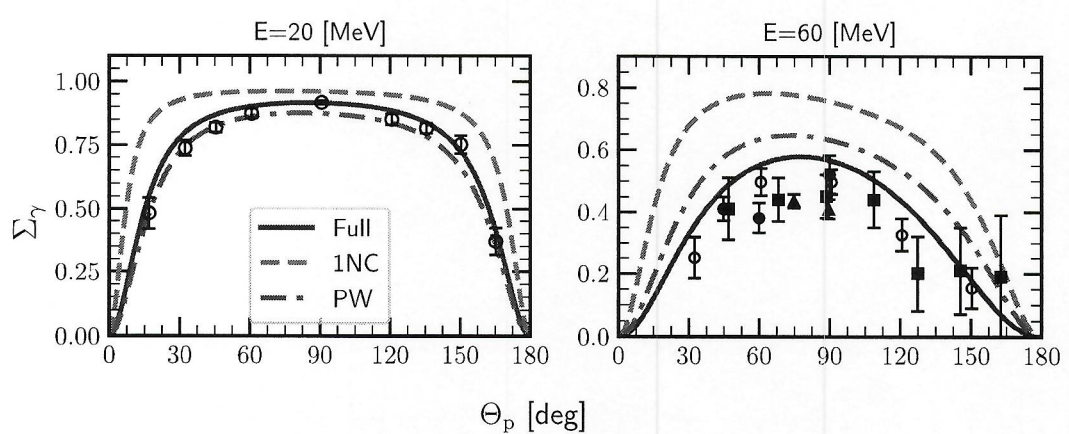


Figure 3.24: The photon asymmetry Σ_γ as a function of the outgoing proton angle θ_p in the CM frame at $E_\gamma = 20$ MeV (left) and $E_\gamma = 60$ MeV (right). Similarly to Fig. 3.4b predictions obtained with chiral N^4LO^+ potential and $\Lambda = 450$ MeV are presented for three theoretical models. The blue solid line is the most complete prediction we have (plane-wave plus rescattering parts, 1NC + Siegert), the pink dashed line shows predictions obtained with single-nucleon current only (1NC) - without the Siegert contributions and the green dashed-dotted line is a prediction in which we neglect the rescattering part and stick to the plane-wave part only but keeping the Siegert contributions. Filled circles are experimental data from [77], empty circles - from [78], filled squares - from [79] and triangles are from [80].

plane-wave plus rescattering part. but with
 as in some frames you ~~want~~ use abbreviation
 in some not
 suggestion: use everywhere

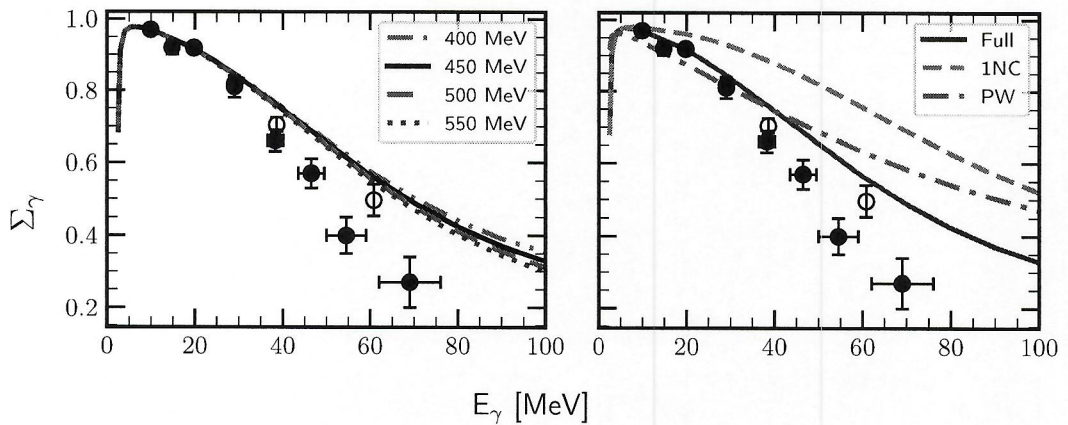


Figure 3.25: The photon asymmetry Σ_γ as a function of the photon energy at the fixed outgoing proton's momentum polar angle $\theta_p = 90^\circ$. On the left panel, each curve corresponds to the particular value of the cut-off parameter and chiral potential used here is the N^4LO^+ one. On the right panel, the blue solid curve represents our most complete predictions comprising the plane-wave plus rescattering parts and 1NC–Siegert current propagator (the same as 450 MeV line in left). The pink dashed curve shows predictions obtained with the single-nucleon current only (without applying the Siegert theorem) and the green dashed-dotted curve represents predictions with the full current (1NC – Siegert) but plane-wave part only. Filled circles are experimental data from [81], empty circles - from [78].

3.2 Helium-3 photodisintegration

3.2.1 Three-body breakup

In this section I will discuss results for ${}^3\text{He} \rightarrow p + p + n$ process differential cross-section ^{for} obtained with ^{???} model of nuclear current. For three free nucleons in the final state, it is convenient to introduce, as a kinematical variable, the arc-length of the S-curve. For a given direction of two momenta \hat{p}_1 and \hat{p}_2 , the S-curve spans in the plane defined by kinetic energies of the same two nucleons, E_1 and E_2 .

For three particles and known initial energy and momenta, five kinematical variables² are required to define the final kinematics. We choose four variables as directions of outgoing nucleons No 1 and 2: $\theta_1, \phi_1, \theta_2$ and ϕ_2 , with the z-axis aligned to the photon momentum. Choosing E_1 as the fifth variable would introduce ambiguity, as in some cases two values of E_2 could be allowed. Instead, the location on the S-curve defines the kinematical configuration unambiguously. The various possible locations of the S-curve in $E_1 - E_2$ plane, as well as the convention on choosing the $S = 0$ point is given in Fig. 1 ^{check} of [18].

In the Fig. 3.28 I demonstrate a differential cross section $\frac{d^5\sigma}{d\Omega_1 d\Omega_2 dS}$ as a function of the S arc-length and as in the previous section, I study the convergence with respect to chiral order and the cut-off dependence. The photon energy is $E_\gamma = 30 \text{ MeV}$; the kinematic configuration $\theta_1 = 15^\circ, \phi_1 = 0^\circ, \theta_2 = 15^\circ, \phi_2 = 180^\circ$ and predictions have been obtained without 3NF.³ On the left, we see that only NLO and N²LO introduce relatively large truncation errors. The maximal width of a band for NLO is 37.6% at $S = 10 \text{ MeV}$, for N²LO it is 12.4% at the same S-value and it is gradually decreasing coming to 0.13% at N⁴LO⁺. The cut-off spread (right) is bigger ^{at} around maxima values but remains below 3%. It reaches 0.78% at the minimum point ($S = 10 \text{ MeV}$).

With larger energy $E_\gamma = 100 \text{ MeV}$, for which predictions are demonstrated in the Fig. 3.29, both truncation error and cut-off spread become larger. The truncation band at the maximum point at $S = 10 \text{ MeV}$ for NLO is 55.0% decreasing to 2.2% at N⁴LO⁺ which still is around 3 times larger than it was for predictions at $E_\gamma = 30 \text{ MeV}$. The cut-off spread also becomes larger with increasing energy value: 9.0% at the same (maximum) point which is also ~ 3 times bigger than the one we observed for the lower energy.

Results for the same $E_\gamma = 100 \text{ MeV}$ but other angular configuration $\theta_1 = 75^\circ, \phi_1 = 75^\circ, \theta_2 = 75^\circ, \phi_2 = 105^\circ$ are given in Fig. 3.30. The top row shows results obtained with 2NF only, while predictions obtained with 3NF are shown on the bottom row. It seems that 3NF does not change much the convergence with respect to the chiral order: truncation error band at the point of maximum $S = 35 \text{ MeV}$ (N⁴LO⁺) is 1.11% and 1.16% with and without 3NF, respectively. As it is almost the same, I conclude that inclusion N²LO 3NF practically does not affect chiral order convergence. Note, 3NF at N²LO has been used for all forces above NLO.

The cut-off dependence, in turn, is affected by the presence of 3NF. Predictions with 2NF only have 13.7% spread at the same maximum point $S = 35 \text{ MeV}$, while predictions with 3NF have only 1.23% relative spread, so the difference is tremendous.

Similar trends are present also in other configurations, demonstrated for the comparison Figs. 3.31, Figs. 3.32 and Figs. 3.33.

²Among nine variables describing final state \vec{p}_1, \vec{p}_2 and \vec{p}_3 , four can be derived from energy and momentum conservation laws.

³Different kinematic configurations $\theta_1, \phi_1, \theta_2$ and ϕ_2 have been tested with a step of 15° and most interesting cases (showing the largest discrepancies) are presented in this work.

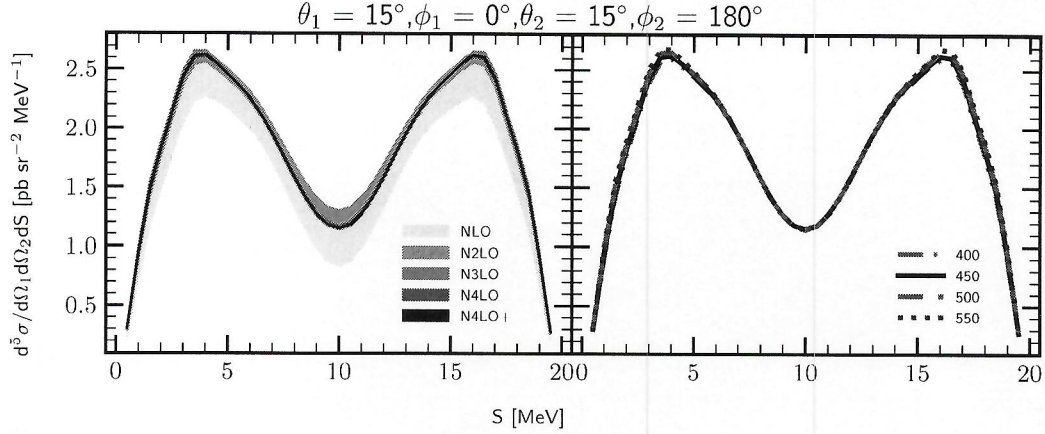


Figure 3.28: The five-fold differential cross section for the photon energy $E_\gamma = 30 \text{ MeV}$ for the kinematic configuration $\theta_1 = 15^\circ, \phi_1 = 0^\circ, \theta_2 = 15^\circ, \phi_2 = 180^\circ$. The left figure presents truncation error bands obtained using the SMS potential with chiral orders from NLO to $N^4\text{LO}^+$, and with cut-off parameter $\Lambda = 450 \text{ MeV}$. The right figure presents a cut-off dependence at $N^4\text{LO}^+$. Results are obtained with two-nucleon force only and 1NC + Siegert current and Siegert theorem used for 2NC contributions. *nuclei*.

The exclusive cross-sections shown above, in Figs. 3.28-3.33 are small and unfortunately below the possibilities of current experimental techniques. The semi-inclusive measurement is more likely to be performed, thus in Figs 3.34 and 3.35 I show the differential cross section $\frac{d^3\sigma}{d\Omega_p dE_p}$. I choose the same photon energies as above: $E_\gamma = 30 \text{ MeV}$ and $E_\gamma = 100 \text{ MeV}$. Each figure consists of subfigures where each row presents results for a proton momenta polar angle $\theta_p = 10^\circ, 50^\circ, 90^\circ, 130^\circ$ and 170° . The left part of each subfigure shows detected chiral order dependence while the right - the cut-off dependence.

At the photon energy 30 MeV the chiral dependence is relatively weak: at the maximum point ($E_p \simeq 3.8 \text{ MeV}$) the relative difference varies between 12 % and 28 % at LO for different angles. This difference decreases with each subsequent order resulting in maximum 0.15 % at $N^4\text{LO}^+$. At the energy $E_\gamma = 100 \text{ MeV}$ truncation errors are larger: at the maximum around $E_p \simeq 1.46 \text{ MeV}$ the discrepancy is around 40 % (NLO), 15 % (N2LO), coming to 1.5 % at $N^4\text{LO}^+$.

A typical cut-off uncertainty at $E_\gamma = 30 \text{ MeV}$ is around 2 % and at $E_\gamma = 100 \text{ MeV}$ increases up to 8 % for all angles and at the same values of E_p as regarded above.

Observed small uncertainties allow me to conclude that the semi-inclusive cross-section $\frac{d^3\sigma}{d\Omega_p dE_p}$ is not useful in studies aiming on pin-down the details of the chiral force. *do we have prediction with other current?*

$N^4\text{LO}^+$

rethinking

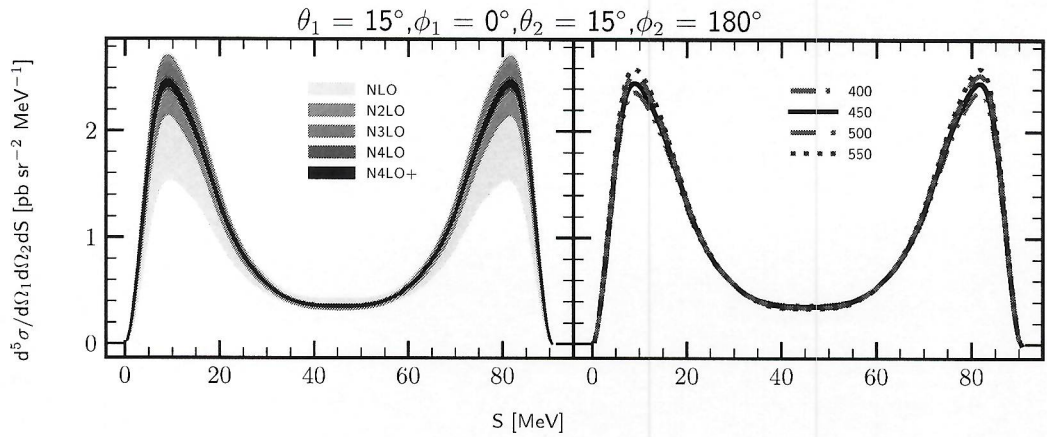


Figure 3.29: The same as in Fig. 3.28 but for the photon energy $E_\gamma = 100 \text{ MeV}$

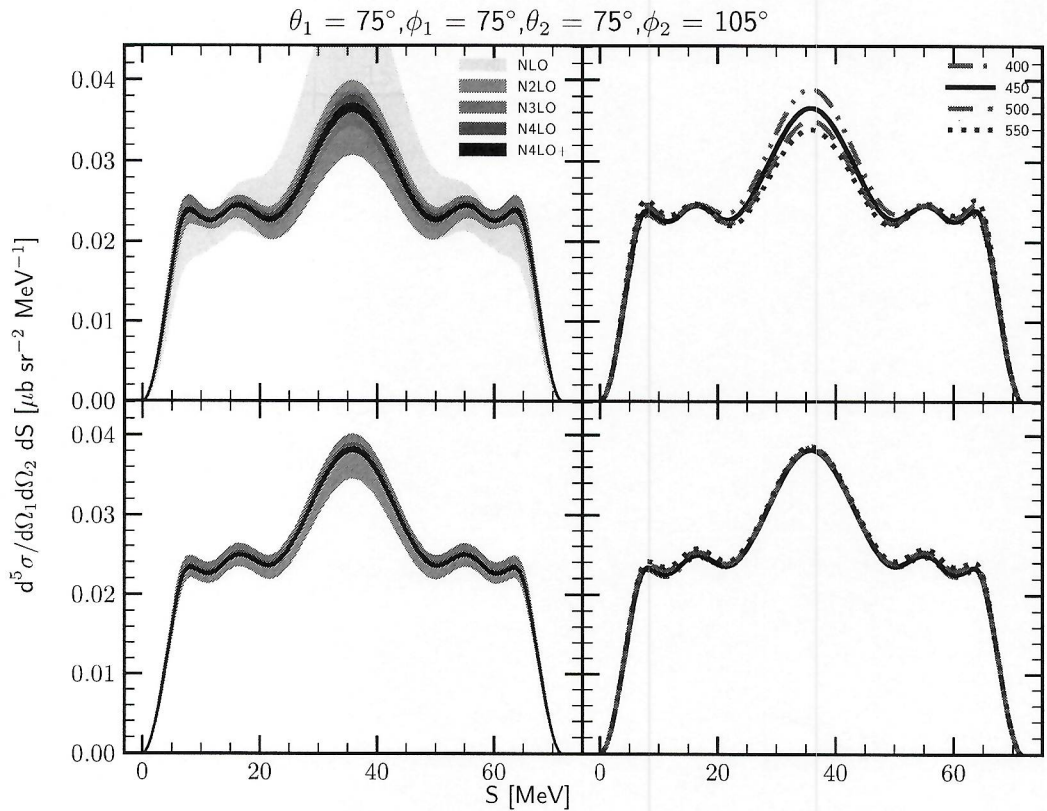


Figure 3.30: The same as in the Fig. 3.29 but for the kinematic configuration at $\theta_1 = 75^\circ$, $\phi_1 = 75^\circ$, $\theta_2 = 75^\circ$ and $\phi_2 = 105^\circ$. Results obtained with the chiral SMS 2N force are presented on the top row. The same, but with the N^2LO 3NF included is presented on the bottom row (starting from the N^2LO - where 3NF appears for the first time).

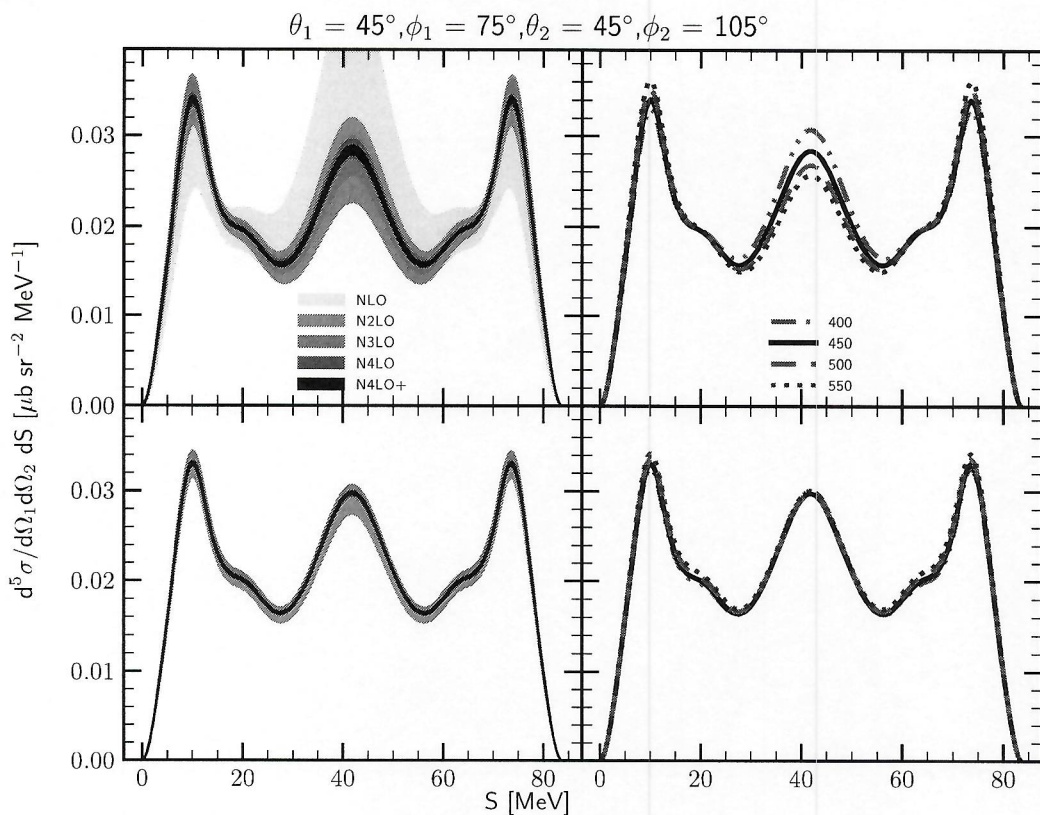


Figure 3.32: The same as in the Fig. 3.31 but for the different kinematic configuration.

described like in ~~Fig. 3.31~~
previous figure

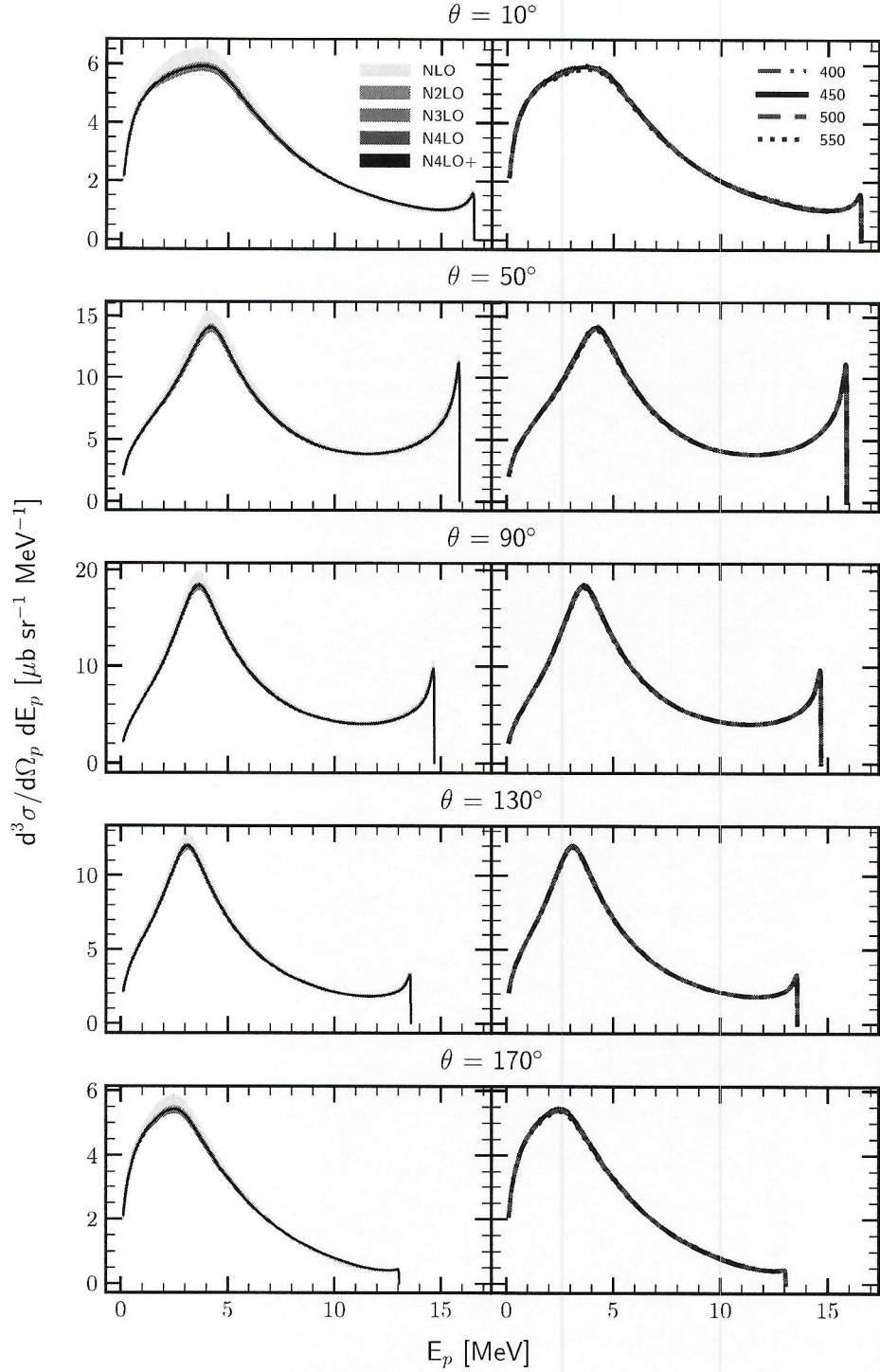


Figure 3.34: The semi-inclusive differential cross section $\frac{d^3\sigma}{d\Omega_p dE_p}$ at $E_\gamma = 30 \text{ MeV}$ $\phi_1 = 0^\circ$ as a function of outgoing proton energy E_p . Each row represents predictions for different values of the outgoing proton's momentum polar angle θ_p : 10° , 50° , 90° , 130° and 170° . The left figure presents truncation error bands obtained using the SMS potential with chiral orders from NLO to $N^{4\text{LO}}+$, and with cut-off parameter $\Lambda = 450 \text{ MeV}$. The right figure presents a cut-off dependence at $N^{4\text{LO}}+$. Predictions have been obtained with the SMS NN potential but neglecting 3NF.

3.2.2 Two-body breakup

The differential cross section $d\sigma/d\Omega_d$ for the ${}^3\text{He} + \gamma \rightarrow d + p$ reaction is presented in the Fig. 3.36 (for the photon energy $E_\gamma = 30 \text{ MeV}$) and in the Fig. 3.37 (for $E_\gamma = 100 \text{ MeV}$). We see a significant enlargement of both truncation and cut-off uncertainties with increasing photon energy. The relative spread of the truncation error at the maximum point ($\theta_p = 105^\circ$) for the lower energy is 0.05 % at N^4LO^+ , while for the larger energy similar spread is 0.45 % (at N^4LO^+ , $\theta_p = 120^\circ$).

The cut-off dependence is also stronger for the larger energy: it is 1.45 % at 30 MeV and 4.01 % at 100 MeV (at the points of maximum).

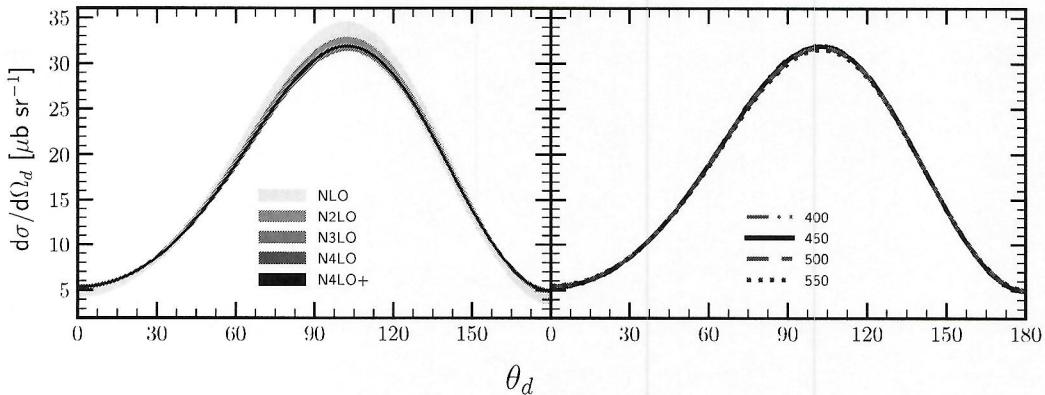


Figure 3.36: Differential cross section for the two-body photodisintegration of ${}^3\text{He}$ as a function of the $d - \gamma$ angle in c.m.. The initial photon energy $E_\gamma = 30 \text{ MeV}$ and NN with 2NF was used.

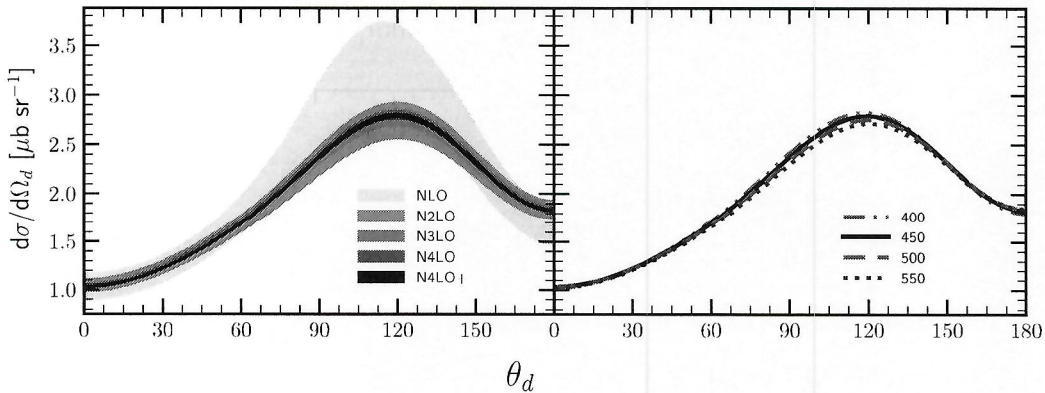


Figure 3.37: The same as in the Fig. 3.36 but for the photon energy $E_\gamma = 100 \text{ MeV}$. C

3.3 Triton photodisintegration

In this section, I will discuss results for ${}^3\text{H} \rightarrow n + n + p$ process in the case when two neutrons are detected and similarly to the previous chapter, I present the convergence of predictions and their cut-off dependence.

In the Fig. 3.38 I present a differential cross section $\frac{d^5\sigma}{d\Omega_1 d\Omega_2 dS}$ as a function of the S arc-length. The photon energy is $E_\gamma = 30 \text{ MeV}$ and the kinematic configuration $\theta_1 = 15^\circ$, $\phi_1 = 0^\circ$, $\theta_2 = 15^\circ$, $\phi_2 = 180^\circ$; predictions have been obtained without 3NF. We see that only NLO and N²LO introduce relatively large truncation errors. The maximal width of a band for NLO is 30.95 % at $S = 10 \text{ MeV}$, for N²LO it is 6.79 % at the same point and it is gradually decreasing coming to 0.10 % at N⁴LO⁺. The cut-off spread around maxima values is 6.25 % (at $S = 4 \text{ MeV}$) and it is 1.81 % at $S = 10 \text{ MeV}$.

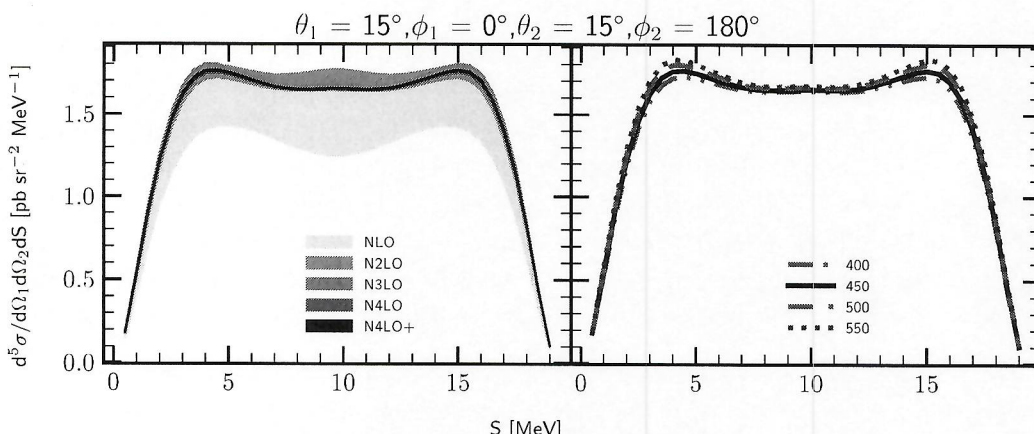


Figure 3.38: The five-fold differential cross section for the photon energy $E_\gamma = 30 \text{ MeV}$ for the kinematic configuration $\theta_1 = 15^\circ$, $\phi_1 = 0^\circ$, $\theta_2 = 15^\circ$, $\phi_2 = 180^\circ$ with two neutrons detected *check ???*. The left figure presents truncation error bands obtained using potential with chiral orders from NLO to N⁴LO⁺, and with cut-off parameter $\Lambda = 450 \text{ MeV}$. The right figure presents a cut-off dependence at N⁴LO⁺. Results are obtained with two-nucleon force only and 1NC current plus Siegert model of nuclear current.

At bigger energy, $E_\gamma = 100 \text{ MeV}$, demonstrated in the Fig. 3.39, the truncation band at the maximum point $S = 10 \text{ MeV}$ for NLO is 50.26 % decreases to 2.00 % at N⁴LO⁺. The cut-off spread also becomes larger with increasing energy value: 9.52 % at the same maximum.

Both The truncation error bands and cut-off dependence are very similar to what was found for the three-body Helium-3 photodisintegration and the relative errors have similar magnitudes.

Results for other angular configurations with $E_\gamma = 30 \text{ MeV}$ and at $\theta_1 = 75^\circ$, $\phi_1 = 75^\circ$, $\theta_2 = 75^\circ$, $\phi_2 = 105^\circ$ are demonstrated in Fig. 3.40. Both truncation errors and cut-off dependence are smaller with such configuration: the relative width of the truncation band at NLO is 9.39 % (at the maximum point $S = 8 \text{ MeV}$) and drops to only 0.1 % at N⁴LO⁺. The relative cut-off spread is 0.93 % at the same point.

At the bigger energy, $E_\gamma = 100 \text{ MeV}$, demonstrated in Fig. 3.41 uncertainties grow. The truncation bands are 44.42 % and 2.09 % (at NLO and N⁴LO⁺ respectively) and the cut-off spread is 13.04 % (all at $S = 35 \text{ MeV}$ in maximum).

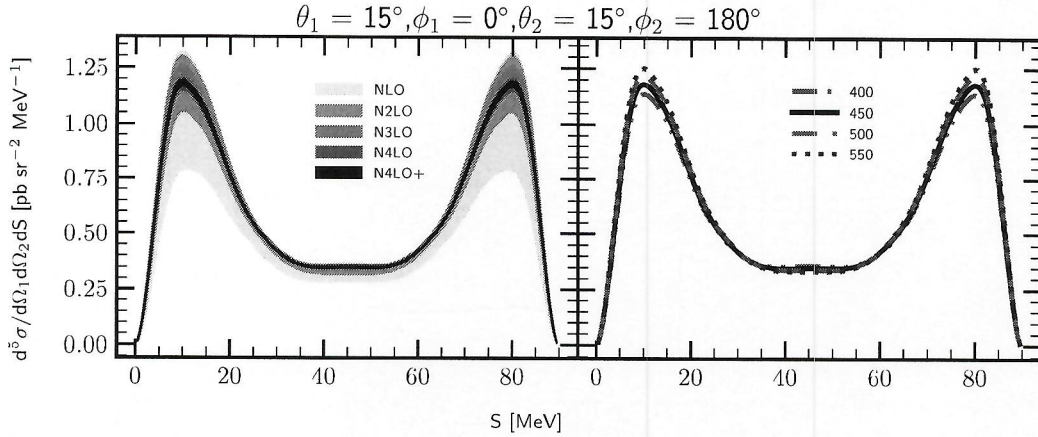


Figure 3.39: The same as in the Fig. 3.38 but for the photon energy $E_\gamma = 100 \text{ MeV}$.

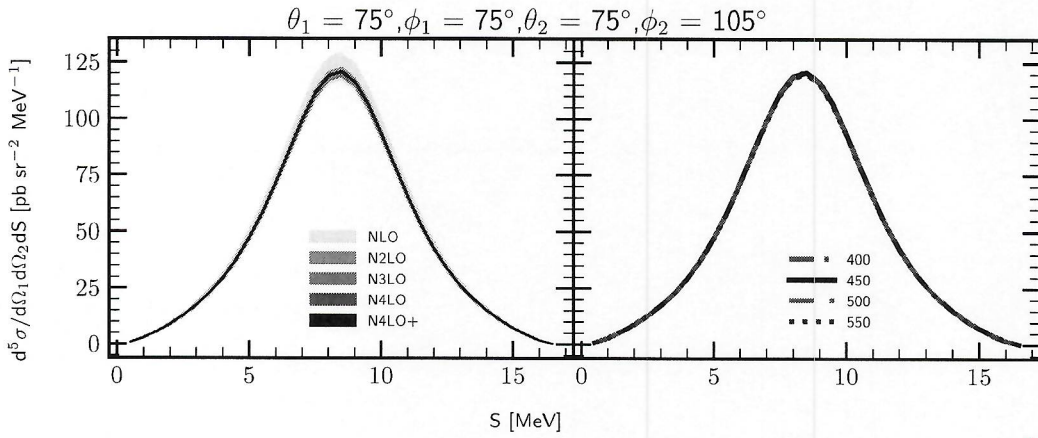


Figure 3.40: The same as in the Fig. 3.38 but for the kinematic configuration with $\theta_1 = 75^\circ, \phi_1 = 75^\circ, \theta_2 = 75^\circ, \phi_2 = 105^\circ$. defined by ↩

Similar trends are present also in other examples, demonstrated for the comparison in Figs. 3.42-3.47. ← ↩

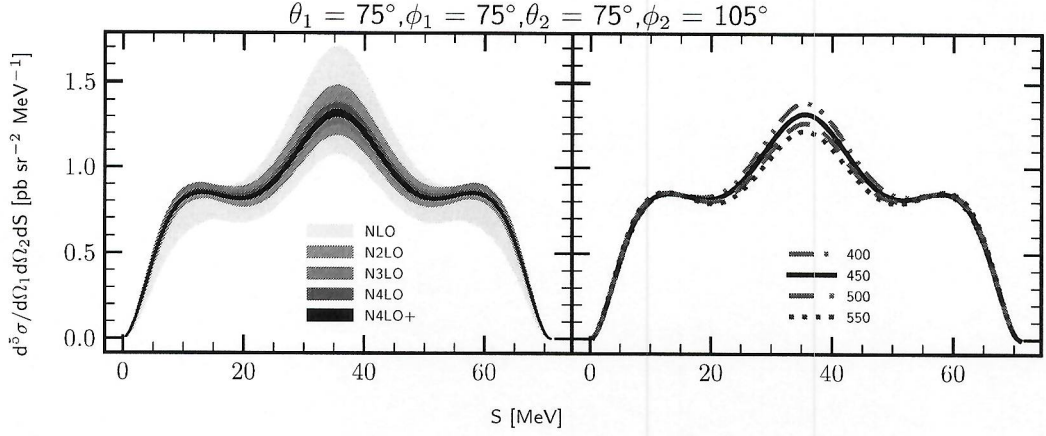


Figure 3.41: The same as in the Fig. 3.40 but for the photon energy $E_\gamma = 100 \text{ MeV}$.

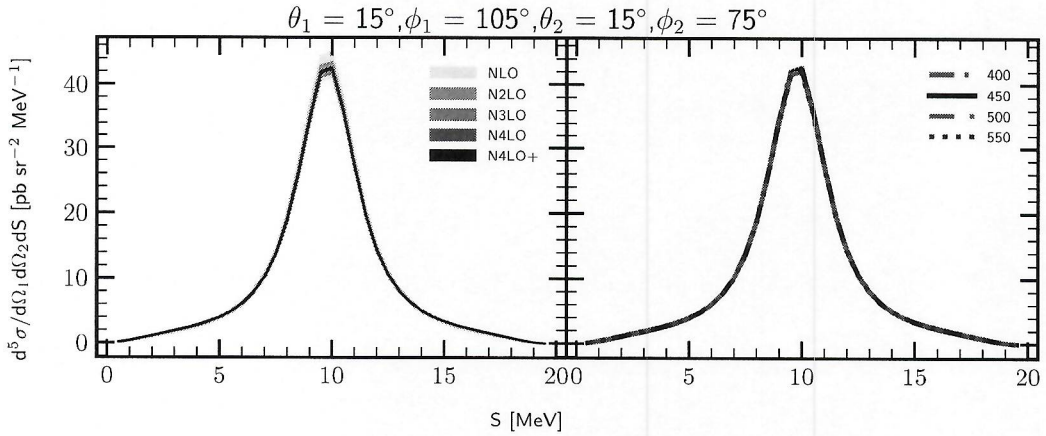


Figure 3.42: The same as in the Fig. 3.40 but for the kinematic configuration with $\theta_1 = 15^\circ, \phi_1 = 105^\circ, \theta_2 = 15^\circ, \phi_2 = 75^\circ$. defined by

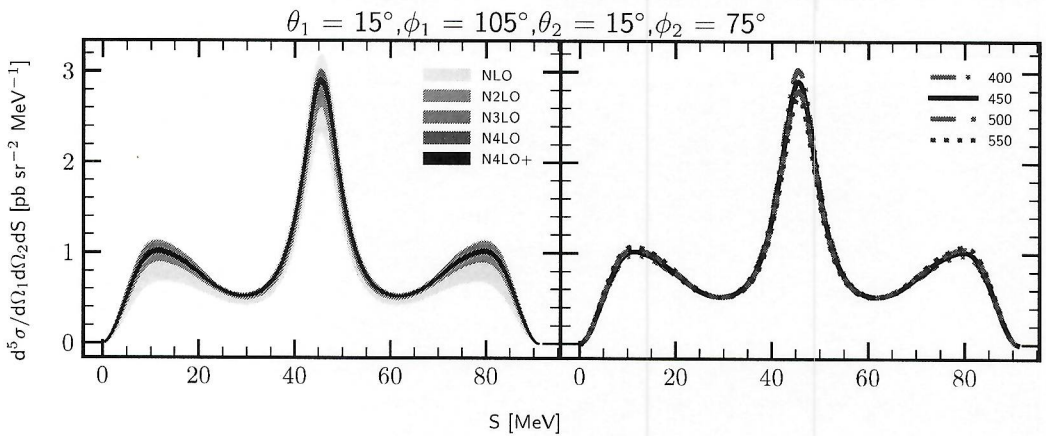


Figure 3.43: The same as in the Fig. 3.42 but for the photon energy $E_\gamma = 100 \text{ MeV}$.

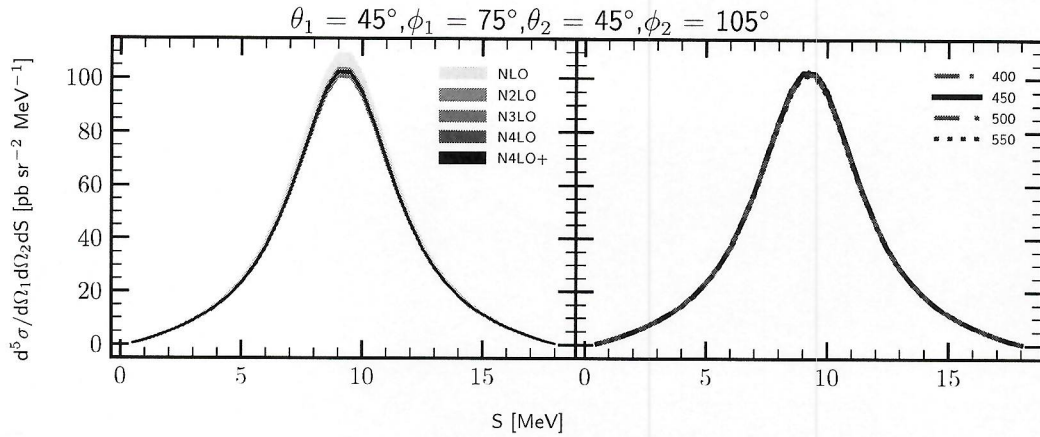


Figure 3.44: The same as in the Fig. 3.42 but for the kinematic configuration with $\theta_1 = 45^\circ, \phi_1 = 75^\circ, \theta_2 = 45^\circ, \phi_2 = 105^\circ$. defined by

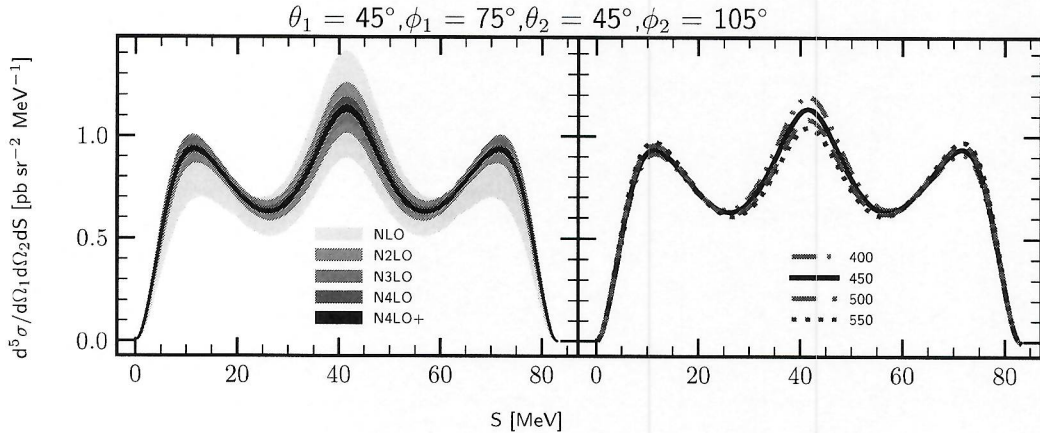


Figure 3.45: The same as in the Fig. 3.44 but for the photon energy $E_\gamma = 100$ MeV. defined by

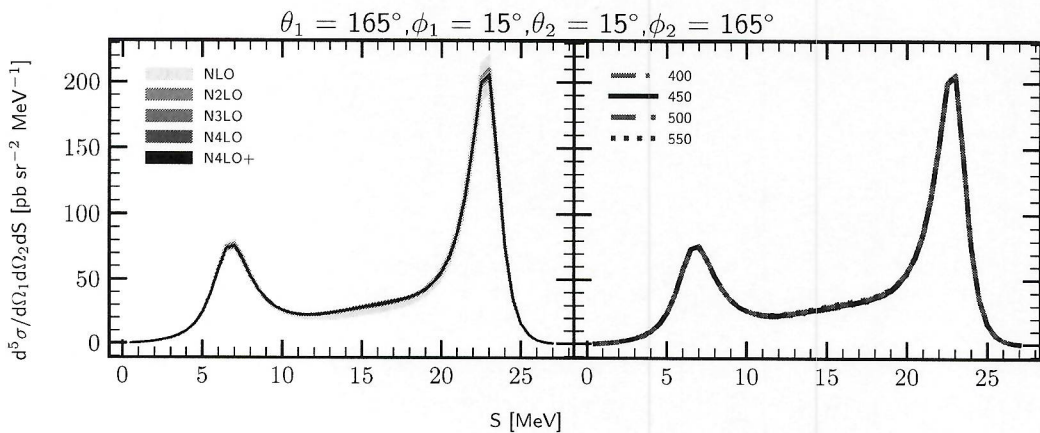


Figure 3.46: The same as in the Fig. 3.44 but for the kinematic configuration with $\theta_1 = 165^\circ, \phi_1 = 15^\circ, \theta_2 = 15^\circ, \phi_2 = 165^\circ$. defined by